ACS Catalysis
Research Article
pubs.acs.org/acscatalysis

Enhanced Visible Activities of α-Fe_2O_3 by Coupling N-Doped Graphene and Mechanism Insight

Lumei He, Liqiang Jing,* Yunbo Luan, Lei Wang, and Honggang Fu*

Key Laboratory of Functional Inorganic Materials Chemistry, School of Chemistry and Materials Science, Heilongjiang University, Ministry of Education, Harbin 150080, People's Republic of China

Ⓢ *Supporting Information*

ABSTRACT: In this work, we first have prepared graphene doped with different amounts of N through a one-pot ammonia-modified hydrothermal process and then successfully coupled them with nanocrystalline α-Fe_2O_3 by a common wet-chemical method. On the basis of the atmosphere-controlled surface photovoltage spectra, time-resolved surface photovoltage responses, and photoinduced hydroxyl radical amount measurements, it is confirmed that the photogenerated charge separation of α-Fe_2O_3 could be enhanced in N_2 or in air atmosphere after coupling with a certain ratio of graphene. It is especially obvious with the graphene doped with a proper amount of nitrogen. This is responsible for the obviously improved visible activities of α-Fe_2O_3 for photoelectrochemical water oxidation to produce O_2 and photocatalytic degradation of gas-phase acetaldehyde and liquid-phase phenol after coupling graphene doped with a proper amount of N species. It is suggested for the first time, mainly by means of N1s XPS data, electrochemical impedance spectra, O_2 temperature-programmed desorption curves, surface acidity-related pyridine-adsorbed FT-IR spectra, and electrochemical O_2 reduction measurements, that the increased amount of doped quaternary-type N would be quite favorable for photogenerated charge transfer and transportation and for O_2 adsorption. As a result, photogenerated charge separation of the resulting N-doped graphene−Fe_2O_3 nanocomposite is greatly promoted. In addition, the enhanced O_2 adsorption of α-Fe_2O_3 results mainly from the increased surface acidity after coupling with graphene, especially with quaternary-type N-doped graphene. This work would help us to better understand the important roles of doped N in graphene in the fabricated nanocomposites and also provide us with a feasible route to improve visible photocatalytic activities of α-Fe_2O_3 greatly.

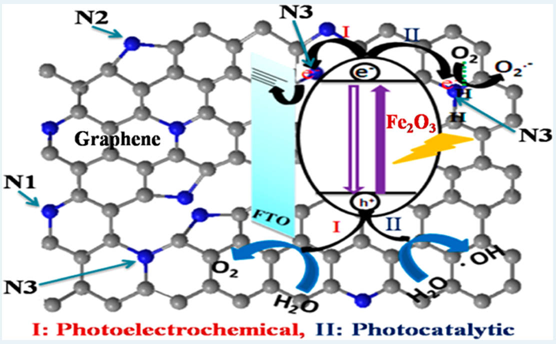

KEYWORDS: *α-Fe_2O_3, N-doped graphene-coupled Fe_2O_3, photogenerated charge separation, photoelectrochemical water oxidation, visible photocatalysis*

1. INTRODUCTION

With the continuous consumption of fossil fuels and increasingly serious environmental pollution, development of novel renewable techniques for energy and environmental issues in the global world[1,2] is highly desirable. As a kind of clean unlimited power, solar energy is gradually becoming more and more important.[3] Accordingly, effective application of solar energy has been considered a feasible strategy to realize renewable production of chemical fuels and complete purification of polluted environments.[4,5] In particular, semiconductor photocatalysis technology, with several merits of high-degree mineralization, mild reaction conditions, and low cost,[6,7] has been widely used as a promising approach in energy production and environmental purification.[8,9] Visible light is about 44% of the solar spectrum. Hence, the key to this technique for widely practical application is to develop inexpensive, steady, and efficient photocatalysts under visible irradiation. Among various visible-spectrun-active oxide semiconductors, α-Fe_2O_3 with a narrow bandgap of 2.1 eV is characterized by several advantages:[10] strong visible absorption, high physical and chemical stability, nontoxicity, environmental compatibility, rich source, and low cost;[11] therefore, in recent years, it has increasingly attracted wide attention in photocatalysis for splitting water and degrading pollutants.[12,13]

However, α-Fe_2O_3 is not an ideal photocatalytic material because of its low quantum efficiency. This is usually ascribed to the short hole diffusion length (about 2−4 nm) and the low conduction band position of Fe_2O_3.[14,15] It is widely accepted that it is favorable to decrease the nanoparticle size of Fe_2O_3 according to the short hole diffusion length, whereas for the low conduction band position, it is beneficial to employ an outer bias. In addition, to date, a great deal of effort has been made toward improving the photocatalytic performance of α-Fe_2O_3.[16,17] In particular, to couple with other substances to fabricate a Fe_2O_3-based nanocomposite, such as with SnO_2, Pd, carbon quantum dots (CQD), and graphene, is often taken as a

Received: November 27, 2013
Revised: February 6, 2014
Published: February 7, 2014

dx.doi.org/10.1021/cs401122e

feasible route for efficient photocatalysis.[18−20] Yu et al. demonstrated that the CQD/α-Fe_2O_3 composite exhibited an enhanced visible photocatalytic activity.[20] It is usually assumed that the enhanced activity is attributed to the improved separation of photogenerated charges. Unfortunately, it is still needed to provide direct evidence. In addition, the role of adsorbed O_2 is often neglected, although the adsorption of oxygen and its capturing photoelectrons are crucial steps in photocatalytic processes occurring at the oxide surfaces.[21]

As a new two-dimensional (2D) system,[22] graphene has been widely used in physical and chemical fields because of its high electrical conductivity, superior electron mobility, and extremely large specific surface area.[23,24] There have been many reports about the enhanced photocatalytic activities by coupling graphene;[25,26] however, seldom has using graphene to improve photocatalytic performance of α-Fe_2O_3 been investigated. In our recent work, it is demonstrated that the introduction of graphene could slightly enhance the photocurrent density and the photocatalytic activity of α-Fe_2O_3 under visible irradiation.[27] It is worth noting that doping heteroatoms could change the physiochemical properties of nanostructured carbons, such as carbon nanotube and graphene, further improving their performances, according to theoretical and experimental studies.[28−30] Among those heteroatoms doped, much attention has been paid to the nitrogen atom because it could noticeably enhance the electrochemical reduction currents of oxygen, for which it is highly desired in the application of fuel cells.[31,32] It is often assumed, lacking direct evidence, that the enhanced electrochemical reduction currents of N-doped graphene are attributable to the increase in the charge transportation capacity and in the adsorbed O_2 amount.[33,34]

Generally speaking, N doped into graphene is involved with mainly three kinds of chemical forms with increasing binding energy, including pyridinic N, pyrrolic N, and quaternary N. Pyridinic N and pyrrolic N would devote one and two p electrons to the p-conjugated systems in the graphene layer, respectively. For quaternary N, it would take the place of the C atom of the hexagonal ring of graphene.[35] Hence, it is expected that, among three N doped species, the quaternary one would have the greatest effect on the properties of graphene. Unfortunately, that is not completely true. It was reported that both pyridinic N and quaternary N could promote the oxygen reduction reactions.[36,37] This is possibly related to their promotion of O_2 adsorption. However, that still needs to be further clarified. In addition, it was reported that the photocatalytic performance for MO dye bleaching and hydrogen evolution from water of semiconductors could be improved after coupling with N-doped graphene.[38,39] Surprisingly, Fe_2O_3 has not been employed for photocatalysis, to the best of our knowledge. In addition, the roles of doped N species are still ambiguous. On the basis of the above considerations, we try to couple N-doped graphene to nanocrystalline α-Fe_2O_3 to greatly enhance its visible photocatalytic activities for water splitting and colorless pollutant degradation. Meanwhile, the activity-enhanced mechanisms would be much revealed by investigating in detail the effects of different doped N species on photogenerated charge behavior and adsorbed O_2 amounts of Fe_2O_3. Obviously, it is of great significance from a scientific or engineering point of view for Fe_2O_3 photocatalysis under visible irradiation.

Herein, it is clearly demonstrated that the visible activities of α-Fe_2O_3 for photoelectrochemical water oxidation to produce O_2 and photocatalytic degradation of gas-phase acetaldehyde and liquid-phase phenol are improved after coupling with graphene, especially with that doped with a proper amount of N species. It has been well confirmed that the obviously improved visible activities are attributable to the greatly enhanced separation of photogenerated charges in N_2 or in air. Interestingly, it is suggested for the first time that the increased amount of doped quaternary-type N would be very favorable for photogenerated charge transfer and transportation and for O_2 adsorption, further leading to the greatly increased charge separation in the resulting N-doped graphene−Fe_2O_3 nanocomposite, and that the enhanced O_2 adsorption of α-Fe_2O_3 mainly depends on the increased surface acidity after coupling with quaternary-type N-doped graphene. This work would help us to better understand the important roles of doped N in graphene in the fabricated nanocomposites and also provide a feasible route to greatly improve the visible photocatalytic activities of α-Fe_2O_3.

2. EXPERIMENTAL SECTION

All the reagents used in this work were of analytical grade and used as received without further purification, and deionized water was employed in all experiments.

2.1. Syntheses of Materials. Graphene (G) was prepared by introducing aqueous $FeCl_2$ to active carbon and stirring for 10 h under the protection of nitrogen, followed by carbonization at 1100 °C under a N_2 atmosphere for 30 min, and treatment in 10% hydrochloric acid at 90 °C for 8 h.[40] The N-doped graphene (NG) was synthesized via a one-pot hydrothermal method employing different amounts of urea as the origin of the doped N in the presence of a graphene-dispersed solution.[41] Nanocrystalline α-Fe_2O_3 (F) was synthesized by a phase-separated hydrolysis-solvothermal method.[42] The composites between graphene and Fe_2O_3 and between N-doped graphene and Fe_2O_3, respectively named as G−F and NG−F, were fabricated by a simple wet chemical processes. Typically, 1.0 g of nanocrystalline α-Fe_2O_3 and 30 mg of G (or NG) were mixed in a 50% ethanol solution under stirring for 3 h, followed by drying at 80 °C and then sintering at 400 °C for 2 h.

2.2. Preparation of Film Electrodes. Conductive fluorine-doped tin oxide (FTO)-coated glasses were used as the substrates for the films. These glasses were washed by deionized water under sonication for 30 min and then cleaned using ethanol and deionized water in turn, followed by thermal treatment at 450 °C for 30 min prior to use. For F, G−F, and NG−F films, the corresponding pastes were prepared as follows: 0.5 g of the resulting powder was dispersed in 2 mL of isopropyl alcohol under vigorously stirring, and then 0.3 g of Macrogol-6000 was introduced to the obtained mixture, followed by an ultrasonic process for 30 min and then stirring for 30 min. Finally, 0.15 mL of acetylacetone was added, and the mixture was then continuously stirred for 2 days, which led to the paste formation. The films were prepared by the doctor blade method, and Scotch tape was adopted as the spacer. After it was naturally dried, the film was calcined at 450 °C for 30 min and then cooled to room temperature. The film was cut into 1.0×2.5 cm^2 pieces, a working geometric surface area of 1.0×1.0 cm^2 containing an illumination area of 0.7×0.7 cm^2, and the remaining area was covered by epoxy resin. To fabricate an electrode, an electrical contact was manufactured with FTO substrates, and silver conducting paste was used to

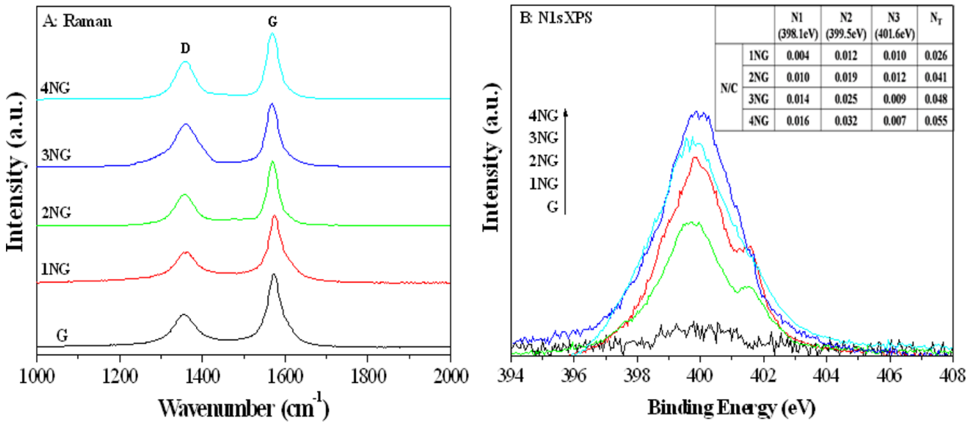

		N1 (398.1eV)	N2 (399.5eV)	N3 (401.6eV)	N_T
N/C	1NG	0.004	0.012	0.010	0.026
	2NG	0.010	0.019	0.012	0.041
	3NG	0.014	0.025	0.009	0.048
	4NG	0.016	0.032	0.007	0.055

Figure 1. Raman spectra (A), and N 1s XPS spectra (B) with an inserted table showing the specific N amount of N1, N2, N3, and the total N amount (N_T) of different NG samples.

connect with a copper wire, which was then sealed in a glass tube.

2.3. Characterization of Materials. The samples were characterized by X-ray diffraction (XRD) with a Rigaku D/MAX-rA diffractometer (Japan) using Cu Kα radiation (α = 0.15418 nm). An accelerating voltage of 30 kV and emission current of 20 mA were employed. Raman spectra were recorded on a Jobin Yvon HR800 micro-Raman spectrometer with 457.9 nm laser, and the laser intensity at the sample was kept below the threshold for any laser-induced changes in the Raman spectra and electrical transport characteristics. The graphene powder was placed on a clean SiO_2/Si substrate for the Raman measurement. The compositions and elemental chemical states of the samples were examined by X-ray photoelectron spectroscopy (XPS) using a Kratos-Axis Ultra DLD apparatus with an Al (mono) X-ray source, and the binding energies were calibrated with respect to the signal for adventitious carbon (binding energy = 284.6 eV). The UV−vis diffuse reflectance spectra (DRS) of the samples were measured by a Shimadzu model UV-2550 spectrophotometer. The electron micrographs were taken on a JEOL JEM-2010 transmission electron microscope (TEM) operated at 200 kV. The atmosphere-controlled surface photovoltage spectra (SPS) and time-resolved surface photovoltage (TR-SPV) responses were measured with the home-built apparatuses that have been described in detail elsewhere.[43] Temperature-programmed desorption (TPD) curves of oxygen were recorded using a home-built facility, as described previously.[27]

Hydroxyl radical measurement was carried out in 0.001 M coumarin aqueous solution in a quartz reactor of 50 mL containing 50 mg of sample powder. Prior to irradiation, the reactor was magnetically stirred for 30 min to ensure the establishment of an adsorption−desorption equilibrium. After irradiation for 1 h, a certain amount of the solution was transferred into a Pyrex glass cell for the fluorescence measurement of 7-hydroxycoumarin at around 456 nm with 332 nm excitation through a spectrofluorometer (Perkin-Elmer LS55). The surface acidities were characterized by the pyridine-adsorbed FT-IR spectra using a PerkinElmer Spectrum 100 spectrometer. Samples were subjected to a conditioning treatment in situ in advance, which involved outgassing at 200 °C for 2 h (residual pressure at 1.33×10^{-2} Pa) and then with cooling to room temperature and equilibrating with pyridine for 15 min. After heating at 150 °C for 0.5 h, recording of the FT-IR spectra began.

2.4. Photoelectrochemical (PEC) Experiments. PEC experiments were performed in a quartz cell using a 500 W xenon light with a stabilized current power supply as the illumination source and 1 M NaOH solution as the electrolyte. The as-prepared films were used as working electrodes illuminated from the FTO glass side, whose illumination area was about 0.7 × 0.7 cm^2. A platinum plate (99.9%) was used as the counter electrode, and a saturated KCl Ag/AgCl electrode (SSE) was used as the reference electrode. All the potentials in this paper were referred to SSE at 298 K, and applied potentials were controlled by a commercial computer-controlled potentiostat (LK2006A made in China). High-purity N_2 or O_2 gas was employed to bubble through the electrolyte before and during the experiments. For comparison, the related current was also measured in the dark. In addition, electrochemical O_2 reduction experiments were carried out in the dark.

To measure the produced O_2 amount in the PEC water oxidation, the as-prepared films were used as working electrodes in a sealed quartz cell with 80 mL of 0.5 M $NaSO_4$ solution as electrolyte, and high-purity nitrogen gas was bubbled through the electrolyte before the experiment. The films were illuminated from the FTO glass side, whose illuminated working area was about 1 × 1 cm^2, at the constant bias of 0.6 V (vs Ag/AgCl). During the experiment, the produced O_2 amount was detected quantitatively with an Ocean Optics fluorescence-based oxygen sensor (NFSC 0058) by putting the needle probe into the electrolyte near the working electrode, and the irradiation lasted for 10 min using a 500 W xenon light with a 420-cutoff filter as the illumination source.

The electrochemical impedance spectroscopy (EIS) was performed with a computer-controlled IM6e impedance measurement unit (Zahner Elektrik, Germany) by applying sinusoidal perturbations of 10 mV with a bias of −0.8 V at the frequency range from 0.05 to 100 kHz. The obtained spectra were fitted with ZsimpWin software on the basis of appropriate equivalent circuits.

2.5. Evaluation of Visible Photocatalytic Activities. The visible photocatalytic activities of the samples were evaluated by degrading gas-phase acetaldehyde and liquid-phase phenol. The light source was a 150 W spherical xenon lamp (XQ150/150 W, Warren Bulb Factory, Shanghai) with an emitting spectrum similar to sunlight, and a light filter was used between the light source and the reactor to cut off UV light

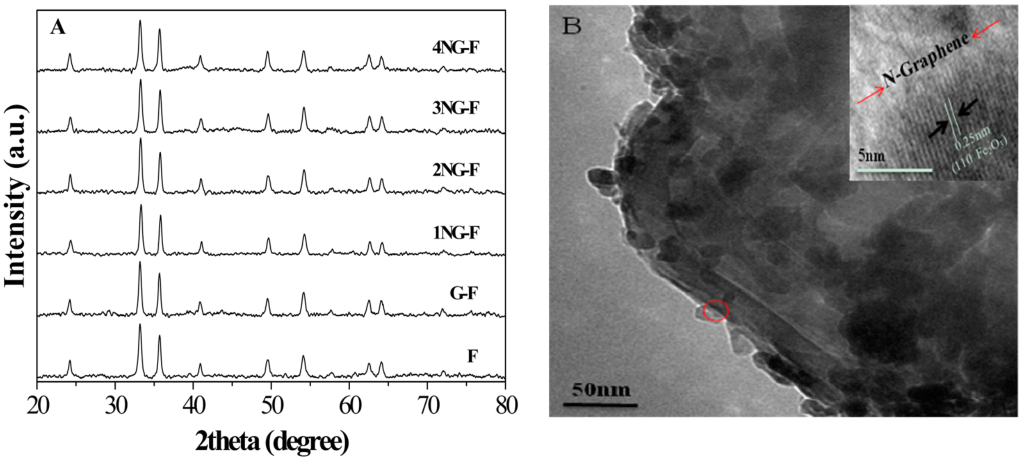

Figure 2. (A) XRD patterns and (B) TEM image with a HRTEM one as the inset of 2NG−F.

(<420 nm) in all photocatalytic experiments. In the gas-phase acetaldehyde degradation experiment, 0.15 g of powder was put into a Pyrex glass cylindrical reactor with a diameter of 7.0 cm and effective volume of 640 mL. A premixed gas containing 810 ppm of acetaldehyde, 20% O_2, and 80% N_2 was introduced into the reactor. The concentration of acetaldehyde for every 20 min time interval was measured with a gas chromatograph (GC-2014, Shimadzu) equipped with a flame ionization detector.

The liquid-phase phenol photocatalytic degradation experiment was carried out in a 100 mL photochemical glass reactor by mixing 0.15 g of powder and 60 mL of 5 mg·L^{-1} phenol solution under magnetically stirring. The light source was placed 15 cm away from the reactor. The reactive system was magnetically stirred in the absence of light for 30 min to keep the adsorption−desorption equilibrium prior to irradiation. The phenol concentration after photocatalytic reactions for 1.5 h was measured by the 4-aminoantipyrine spectrophotometric method at the characteristic optical adsorption (510 nm) of phenol with a Shimadzu UV-2550 spectrophotometer after centrifugation.

3. RESULTS AND DISCUSSION

3.1. Composition and Structural Characterization. One can see from Figure 1A that the Raman spectra of undoped and N-doped graphene exhibit two remarkable bands at around 1340 and 1580 cm^{-1}, assigned to the D and G bands, respectively.[44] The G band is related to graphitic carbon, and the D is associated with the defect in the hexagonal graphitic layer. The high intensity ratio of I_G to I_D reflects the high degree of graphitization.[45] It is calculated that the I_G/I_D value of graphene is 1.78, whereas that of the N-doped one becomes slightly smaller, from 1.73 to 1.62, with an increase in the amount of used urea. This indicates that the graphitization degree of N-doped graphene is a little low compared with that of the undoped one.

According to the N 1s XPS spectra shown in Figure 1B and Supporting Information (SI) Figure S1, along with its relative XPS data as an inserted table, it is confirmed that the N atoms are successfully doped into the skeleton of graphene, and the atomic number ratio of doped N to C gradually becomes large as the amount of used urea is increased. By means of N 1s XPS-peak-differentation-imitating analyses, it is deduced that there are three kinds of N chemical forms in N-doped graphene (NG)—pyridinic N (N1, 398.1 eV), pyrrolic N (N2, 399.5 eV), and quaternary N (N3, 401.6 eV)—with increasing binding energy.[35] One can notice that, similar to the total N, the pyridinic N and pyrrolic N contents gradually become high as the amount of used urea is enhanced. However, the quaternary N content first increases and then begins to decrease, and it is the maximum content (0.012) of quaternary N in the resulting NG when the mass ratio of used urea to graphene is 200:1. For the undoped and N-doped graphene, the C 1s binding energy is 284.6 eV (SI Figure S1), resulting from graphitic carbon, which is consistent with ref 44. On the basis of the TEM images (SI Figure S2), it is confirmed that the resulting graphene possesses a several-layer structure, with slight scrolling at the sheet edges. Noticeably, the doped N species nearly does not affect the graphene structure.

In our previous work,[27] it is clearly demonstrated that the fabricated graphene−Fe_2O_3 nanocomposite exhibits highly visible photocatalytic activity when the mass ratio of graphene to α-Fe_2O_3 is 3:100. Hence, the mass ratio of N-doped graphene to Fe_2O_3 is still kept at 3% in mass in this work. It is shown in Figure 2A that all XRD diffraction peaks are attributed to α-Fe_2O_3 according to the standard card JCPDS 33-0664, and they are nearly not changed after coupling with undoped and N-doped graphene, implying no effects on the phase composition and crystallinity. On the basis of the TEM image (Figure 2B), it is observed that the nanocrystalline α-Fe_2O_3 is spherical with a size of ~16 nm, consistent with the evaluated crystallite size by the Scherrer formula, and is well dispersed on the surfaces of N-doped graphene. Noticeably, the effectively contacted nanocomposites between N-doped graphene and α-Fe_2O_3 are formed by means of the HRTEM image as the inset, on which the crystal facet distance of 0.25 nm results from α-Fe_2O_3.[46] Based on the UV−vis DRS spectra (SI Figure S3), it is confirmed that the optical absorption behavior of α-Fe_2O_3 is not affected by coupling with N-doped graphene.

3.2. Photogenerated Charge Properties. To investigate the properties of photogenerated charges, atmosphere-controlled steady-state surface photovoltage spectra (SS-SPS) are performed first. In general, the surface photovoltage signal of solid semiconductor material results mainly from the photogenerated charges, followed by separation under the built-in electric field or via the diffusion process,[47] and the SPS response of a nanosized semiconductor should originate mainly from the photogenerated charge separation via the diffusion process because the built-in electric field of a nanomaterial is usually neglected.[48] As seen from SI Figure S4, the coupled graphene undoped or doped with N does not change the SPS attribute of α-Fe_2O_3,which shows that O_2 is necessary for the SPS occurrence; the larger the O_2 content, the stronger the SPS response.[49] This is attributed to the O_2 adsorbed on the surfaces easily capturing the photogenerated electrons so as to promote the positive photogenerated holes preferentially diffuse to the surfaces of the testing electrode in the presence of O_2. Interestingly, it is noted from the inset of Figure 3 that the SS-SPS response of α-Fe_2O_3 in N_2 is enhanced after coupling with graphene, especially with the N-doped. This indicates that it is beneficial for the transfer and separation process of photogenerated charges of α-Fe_2O_3 to couple with N-doped graphene. Moreover, it is noticed from Figure 3A that the SS-SPS response of α-Fe_2O_3 in air is obviously increased after a certain ratio of graphene (3% in mass) is coupled, especially for an appropriate amount of the N-doped. For the N-doped graphene-coupled Fe_2O_3 (NG−F), it exhibits the strongest SPS response in air when the mass ratio of used urea to graphene is 200:1, which corresponds to the highest photogenerated charge separation, based on the SPS principle.[47] However, the excess doped-N species would lower the SPS response of the resulting graphene−Fe_2O_3 nanocomposite so as to be unfavorable for photogenerated charge separation.

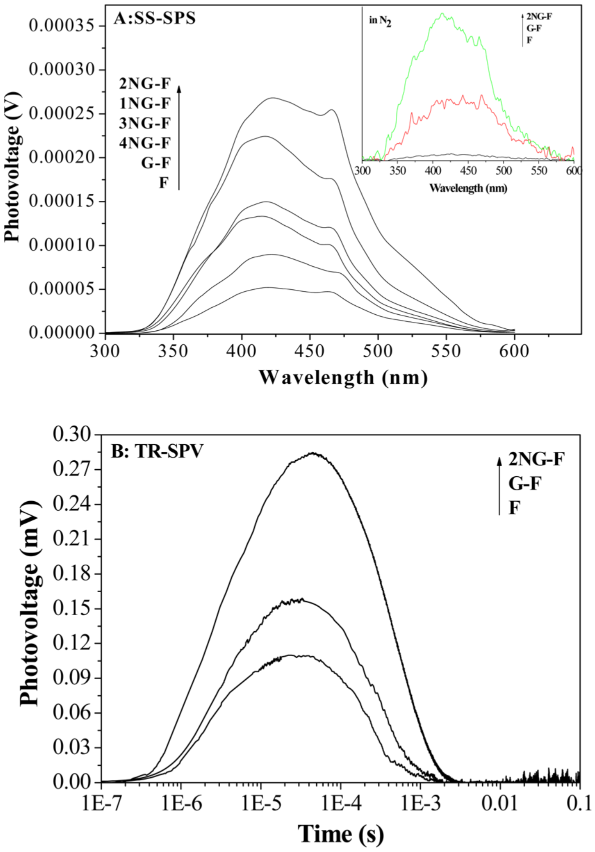

Figure 3. SS-SPS (A) and TR-SPV (B) responses in air. The inset in A shows the SS-SPS responses in N_2 atmosphere.

As expected, the above SS-SPS results are further supported by the time-resolved surface photovoltage (TR-SPV) responses. During the TR-SPV measurements, an ∼10 μm thick mica spacer was placed between the ITO glass and the sample to decrease the space charge region at the ITO−sample interface, and the samples were excited by a 532 nm laser radiation with a 10 ns pulse. For a nanosized semiconductor, its photogenerated charge separation is greatly influenced by the carrier diffusion process, which mainly contributes to the slow photovoltage response ($>10^{-4}$ s frequently).[50] Because the presence of O_2 is favorable for capturing photogenerated electrons, it is understandable that the resulting Fe_2O_3-based nanocomposite should display a positive TR-SPV response via the carrier diffusion process. One can see from Figure 3B that the positive TR-SPV response of α-Fe_2O_3 is increased after coupling a certain amount of graphene, especially for the N-doped graphene (2NG−F), and its charge carrier lifetime is also prolonged on the milliseconds time scale. Obviously, the TR-SPV results are in good accordance with the SS-SPS.

3.3. Visible Photocatalytic Activities for Water Splitting and Pollutant Degradation. On the basis of the above results of SS-SPS and TR-SPV responses, it is concluded that the separation of photogenerated charges of α-Fe_2O_3 is enhanced in N_2 or in air after coupling a certain ratio of graphene, especially for the appropriate amount of N-doped graphene. Thus, it is hypothesized that the fabricated N-doped graphene−Fe_2O_3 nanocomposite would exhibit much high visible photocatalytic activities for water oxidation to produce O_2 and colorless pollutant degradation to purify the environment. As seen from SI Figure S5, the current onset voltage of α-Fe_2O_3 in the dark is slightly shifted to lower potential after coupling with N-doped graphene. However, it is noted from Figure 4A that the visible photocurrent of α-Fe_2O_3 is enhanced,

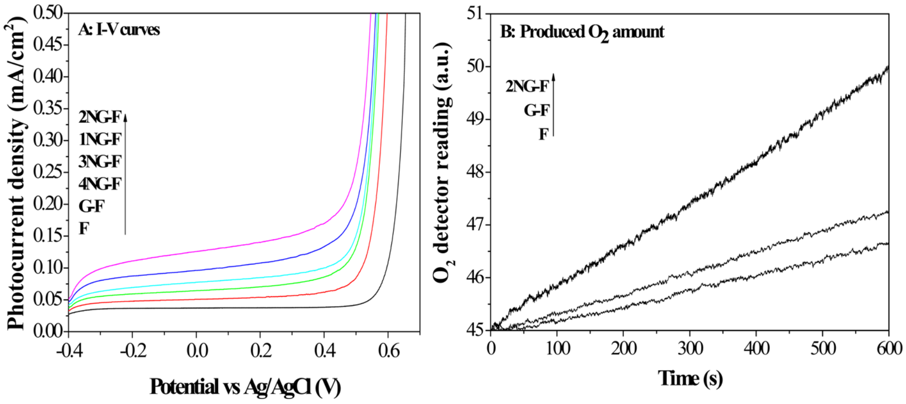

Figure 4. *I*−*V* curves under visible irradiation (A) and the produced O_2 amount (B).

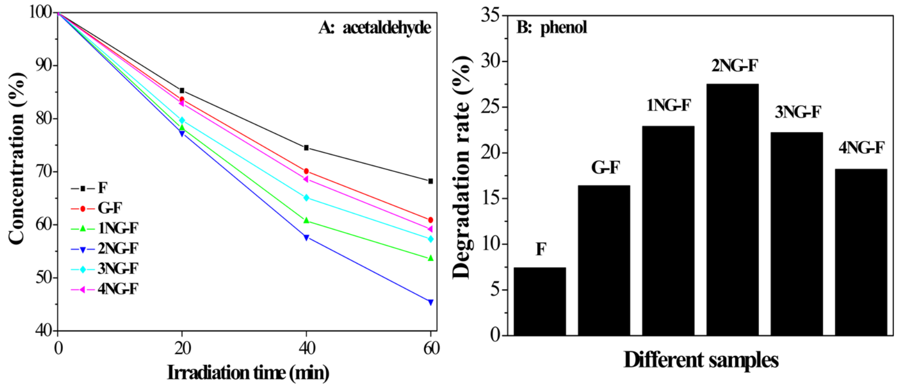

Figure 5. Photocatalytic degradation of gas-phase acetaldehyde (A) and liquid-phase phenol (B) on F, G−F, and different NG−F samples under visible irradiation.

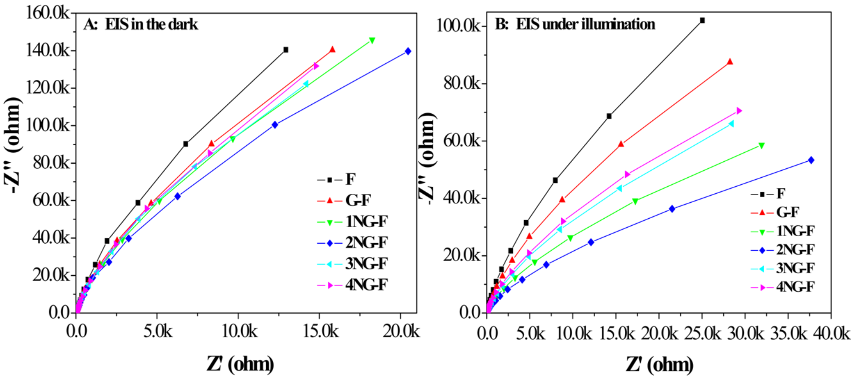

Figure 6. Electrochemical impedance spectra of different samples (A) in the dark and (B) under illumination.

especially for the N-doped graphene-coupled Fe_2O_3, with the same onset voltage of about −0.4 V for all Fe_2O_3-based films. For the 2NG−F nanocomposite, it exhibits the highest photocurrent, with a 4-fold enhancement compared with α-Fe_2O_3. This is further proved by the produced O_2 amount in the photoelectrochemical water oxidation on different Fe_2O_3 films (Figure 4B). It is found that a small amount of O_2 for α-Fe_2O_3 is produced, and its amount of produced O_2 could be increased after coupling with a small ratio of graphene, especially with the appropriate amount of the N-doped one.

To reasonably evaluate visible photocatalytic activities for degrading pollutants, we chose colorless gas-phase acetaldehyde and liquid-phase phenol as the model compounds. As expected, according to Figure 5, it is confirmed that the visible photocatalytic activities for degrading acetaldehyde and phenol of α-Fe_2O_3 is improved after coupling with graphene, especially for that doped with an appropriate amount of N species, and the 2NG−F nanocomposite exhibits the best photocatalytic performance. This is in good agreement with the above activity for water oxidation to produce O_2. By comparison, it is easily noticed that, for the resulting Fe_2O_3-based samples, the stronger the SS-SPS responses, the higher the visible photocatalytic activities. Therefore, it is concluded that the obviously improved visible photocatalytic activities of α-Fe_2O_3 are attributable to the greatly enhanced separation of photogenerated charges after coupling with N-doped graphene. This is further supported by the formed hydroxyl radical amounts on the different Fe_2O_3-based samples after visible irradiation.

It is widely accepted that the hydroxyl radical (·OH) is a key active species in the photocatalytic process[51] and that the coumarin fluorescent method is a highly sensitive technique that is frequently used to detect the amount of produced ·OH, in which the introduced coumarin easily reacts with ·OH to produce luminescent 7-hydroxycoumarin at ~460 nm. A strong fluorescent signal usually indicates a large ·OH amount, corresponding to a high photogenerated charge separation. As seen from SI Figure S6, the produced ·OH amount of α-Fe_2O_3 is increased after coupling with graphene, especially with that doped with an appropriate amount of N species. For the 2NG−F nanocomposite, its produced ·OH amount is the largest among the fabricated ones. This agrees with the above SPS and SPV results.

3.4. Discussion on Mechanism Insights.

On the basis of the above results, it is confirmed that the photogenerated charge separation of α-Fe_2O_3 could be enhanced after coupling with a certain ratio of graphene, especially with that doped with an appropriate amount of N species. What causes the enhanced charge separation? What are the roles of the doped N species in the charge separation? To clarify these issues, we have carried out measurements of electrochemical impedance spectroscopy (EIS), which is a powerful method to evaluate the internal resistances for the charge transportation process of electrode materials.[52] One can see from Figure 6 that the Nyquist plot exhibits one capacitive arc in the dark for all resulting Fe_2O_3-based films, reflecting the charge transfer resistance. In addition, the observed arc radii of α-Fe_2O_3 are slightly decreased after coupling with graphene doped with an appropriate amount of N species, indicating that its charge transfer resistance becomes somewhat smaller. This is responsible for the slight shift to lower potential of the current onset voltage in the dark that was observed above. Interestingly, the capacitive arc radii under illumination are obviously smaller than those in the dark,

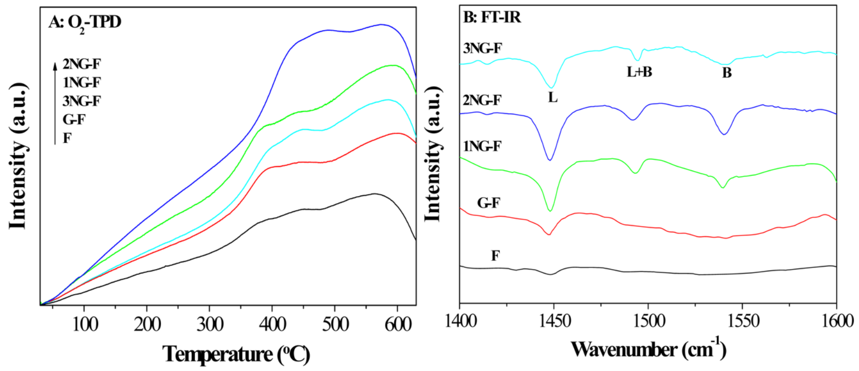

Figure 7. Curves of O_2 temperature-programmed desorption (A) and surface acidity-related pyridine-adsorbed FT-IR spectra (B) of different Fe_2O_3-based samples (L, Lewis acid sites; B, Brönsted acid sites).

especially for the fabricated nanocomposites between N-doped graphene and α-Fe_2O_3, and 2NG−F displays the smallest capacitive arc radii under illumination. This indicates that it is very favorable for photogenerated charge transfer and separation of α-Fe_2O_3 to couple with graphene that is appropriately doped with N, leading to the greatly improved photocurrent.[53]

As described above, the adsorbed O_2 would strongly influence the charge separation by capturing photogenerated electrons, which are crucial for effective photocatalytic degradation of pollutants.[27] Because the photogenerated electrons would transfer from α-Fe_2O_3 to the N-doped graphene in the fabricated nanocomposite, it is expected that the ability of N-doped graphene to adsorb O_2 would greatly influence the final separation situation of photogenerated charges. As for the expectation, we have measured the TPD of O_2, as shown in Figure 7A. In general, the desorbed O_2 at the low and high (over 350 °C) temperature is attributed to the physically and chemically adsorbed forms, respectively.[54] One can notice that the amount of desorbed O_2 of α-Fe_2O_3 is obviously increased after coupling with N-doped graphene, especially for the chemically desorbed form. This is very beneficial for photogenerated charge separation. In addition, the adsorbed O_2 amount of N-doped graphene-coupled Fe_2O_3 is closely related to the quaternary N amount of doped N species. For the 2NG−F nanocomposite, it exhibits a large amount of desorbed O_2, contributing to its strong SPS response. This is further supported by the electrochemical reduction curves of O_2. As seen from SI Figure S7, the O_2 reduction current of α-Fe_2O_3 in the dark is obviously enhanced after coupling with N-doped graphene, and the larger the adsorbed O_2 amount, the higher the O_2 reduction current. This clearly demonstrates that the increased O_2 adsorption corresponds to the high O_2 reduction current.

Why is the adsorbed O_2 amount increased after coupling with N-doped graphene? According to our previous work,[55] in which it is demonstrated that the increased surface acidity is very favorable for O_2 adsorption, it is assumed that the increased O_2 adsorption of α-Fe_2O_3 would be related to the increased acidity after coupling with N-doped graphene. To prove the assumption, the pyridine-adsorbed FT-IR spectra are recorded, as shown in Figure 7 B. The FT-IR peaks at 1450 and 1540 cm^{-1} result from the Lewis and Brönsted acids, respectively.[56] It is confirmed that the surface acidity of α-Fe_2O_3 is greatly strengthened after coupling with N-doped graphene, and the 2NG−F displays very strong surface acidity. Obviously, the strong acidity corresponds to the large amount of adsorbed O_2, which is demonstrated for the N-doped graphene for the first time. Therefore, it is deduced that the increased surface acidity is responsible for the increased O_2 adsorption.

On the basis of the XPS data, SS-SPS and TR-SPV responses, visible photocatalytic activities, produced ·OH amounts, EIS results, adsorbed O_2 amounts and surface acidities, it is worth noting that the photogenerated charge separation situation and visible photocatalytic activities of the resulting Fe_2O_3-based nanocomposites depend mainly on the quaternary N amount in the N-doped graphene. For 2NG, it possesses the largest quaternary N amount in the coupled graphene so as to exhibit the best visible photocatalytic performance. Therefore, it is suggested that it is very favorable for photogenerated charge separation and visible photocatalytic activities of α-Fe_2O_3 to couple with the quaternary-N-doped graphene. For pyridinic N and pyrrolic N doping, their effects are neglectable compared with that of the quaternary N. It is acceptable because the quaternary N replaces the C atom of the hexagonal ring in the graphene, whereas the pyridinic N and pyrrolic N contribute one and two p electrons, respectively, to the p-conjugated systems. On the basis of theoretical study,[57] it is suggested that the doped quaternary N, along with its adjacent C atoms, is helpful for combining with hydrogen so as to greatly increase the surface acidities.

According to the above discussion, a schematic of the visible-spectrum-excited charge transfer and separation process in the fabricated N-doped graphene-coupled Fe_2O_3 is suggested, as shown in Figure 8. For the resulting graphene−Fe_2O_3 nanocomposite, the visible-spectrum-excited electrons of Fe_2O_3 would transfer to the coupled graphene so as to

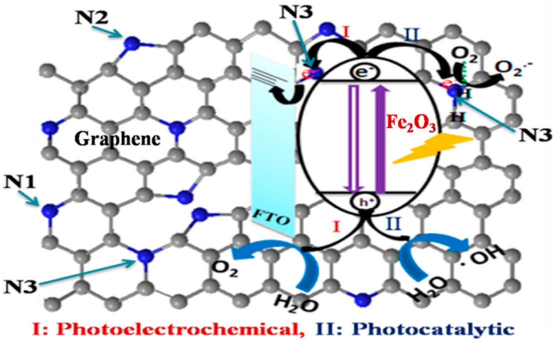

Figure 8. Schematic of photogenerated charge transfer and separation processes in the fabricated N-doped graphene−Fe_2O_3 nanocomposite.

promote charge separation. When the coupled graphene is doped with quaternary N, it is very favorable for the transfer and separation processes of photogenerated charges. In addition, the larger the doped quaternary N amount, the greater the positive effect. Hence, its greatly enhanced charge separation of Fe_2O_3 after coupling with the quaternary-N-doped graphene leads to the obviously improved visible photocatalytic activities for water oxidation to produce O_2 and for colorless pollutant degradation to purify the environment. Moreover, the doped quaternary N is helpful for promotion of O_2 adsorption in the resulting Fe_2O_3-based nanocomposite, which would further contribute to the efficient photocatalysis for degrading pollutants. Compared with the effects of the doped quaternary N, those of the doped pyridinic N and pyrrolic N are neglected.

4. CONCLUSIONS

In this study, graphene−Fe_2O_3 and N-doped graphene−Fe_2O_3 nanocomposites have been fabricated by a simple wet chemical method. The visible activities for photoelectrochemical water oxidation to evolve O_2 and for photocatalytic colorless pollutant degradation to the purify environment are enhanced after coupling with graphene, very obvious for one doped with an appropriate amount of N species. It is clearly demonstrated for the first time that the obviously enhanced visible activities of α-Fe_2O_3 are mainly attributed to the promoted charge transfer and separation, and O_2 adsorption after coupling with a small ratio of N-doped graphene, and the doped quaternary N could play more important roles than the other two N species, pyridinic N and pyrrolic N. Moreover, the increased surface acidity is responsible for the promoted O_2 adsorption due to the introduced quaternary N in the fabricated nanocomposites. This work puts forward new insight into the visible spectrum activity-enhanced mechanisms mainly related to the doped quaternary N in graphene and also provides a new route to design graphene−oxide nanocomposites with high activities for PEC water oxidation and photocatalytic pollutant degradation.

■ ASSOCIATED CONTENT

Supporting Information

Figure S1, XPS spectra; Figure S2, TEM images; Figure S3, UV−vis DRS spectra; Figure S4, SS-SPS responses; Figure S5, $I-V$ curves in the dark; Figure S6, fluorescence spectra related to the formed hydroxyl radical amount; and Figure S7, O_2 electrochemical reduction curves. This material is available free of charge via the Internet at http://pubs.acs.org.

■ AUTHOR INFORMATION

Corresponding Author

*E-mail: Jinglq@hlju.edu.cn.

Notes

The authors declare no competing financial interest.

■ ACKNOWLEDGMENTS

We are grateful for financial support from NSFC (21071048), the Program for Innovative Research Team in Chinese Universities (IRT1237), the Project of Chinese Ministry of Education (213011A), the Specialized Research Fund for the Doctoral Program of Higher Education (20122301110002), and the Chang Jiang Scholar Candidates Programme for Heilongjiang Universities (2012CJHB003).

■ REFERENCES

(1) Lewis, N. S.; Nocera, D. G. *Proc. Natl. Acad. Sci. U.S.A.* **2006**, *103*, 15729.

(2) Kubacka, A.; Fernández-García, M.; Colón, G. *Chem. Rev.* **2012**, *112*, 1555−1614.

(3) Grätzel, M. *Nature* **2001**, *414*, 338−344.

(4) Hoffmann, M. R.; Martin, S. T.; Choi, W.; Bahnemann, D. W. *Chem. Rev.* **1995**, *95*, 69−96.

(5) Luan, Y. B.; Jing, L. Q.; Xie, Y.; Sun, X. J.; Feng, Y. J.; Fu, H. G. *ACS Catal.* **2013**, *3*, 1378−1385.

(6) Mills, A.; Davies, R. H.; Worsley, D. *Chem. Soc. Rev.* **1993**, 417−425.

(7) Fujishima, A.; Honda, K. *Nature* **1972**, *238*, 37−38.

(8) Jing, L. Q.; Zhou, W.; Tian, G. H.; Fu, H. G. *Chem. Soc. Rev.* **2013**, *42*, 9509−9549.

(9) Bai, X. J.; Wang, L.; Zhu, Y. F. *ACS Catal.* **2012**, *2*, 2769−2778.

(10) Sivula, K.; Forma, F. L.; Grätzel, M. *ChemSusChem* **2011**, *4*, 432−449.

(11) Ling, Y. C.; Wang, G. M.; Wheeler, D. A.; Zhang, J. Z.; Li, Y. *Nano Lett.* **2011**, *11*, 2119−2125.

(12) Klahr, B.; Gimenez, S.; Fabregat-Santiago, F.; Bisquert, J.; Hamann, T. W. *Energy Environ. Sci.* **2012**, *5*, 7626−7636.

(13) Hu, Y. S.; Kleiman-Shwarsctein, A.; Stucky, G. D.; McFarland, E. W. *Chem. Commun.* **2009**, 2652−2654.

(14) Kennedy, J. H.; Frese, K. W. *J. Electrochem. Soc.* **1978**, *125*, 709−714.

(15) Klahr, B.; Gimenez, S.; Fabregat-Santiago, F.; Hamann, T. W.; Bisquert, J. *J. Am. Chem. Soc.* **2012**, *134*, 4294−4302.

(16) Luo, J. H.; Maggard, P. A. *Adv. Mater.* **2006**, *18*, 514−517.

(17) Meng, F. K.; Li, J. T.; Cushing, S. K.; Bright, J.; Zhi, M. J.; Rowley, J. D.; Hong, Z. L.; Manivannan, A.; Bristow, A. D.; Wu, N. Q. *ACS Catal.* **2013**, *3*, 746−751.

(18) Uchiyama, H.; Yukizawa, M.; Kozuka, H. *J. Phys. Chem. C* **2011**, *115*, 7050−7055.

(19) Wei, Y. H.; Han, S. B.; Walker, D. A.; Warren, S. C.; Grzybowski, B. A. *Chem. Sci.* **2012**, *3*, 1090−1094.

(20) Yu, B. Y.; Kwak, S. Y. *J. Mater. Chem.* **2012**, *22*, 8345−8353.

(21) Chen, D. W.; Ray, A. K. *Appl. Catal., B* **1999**, *23*, 143−157.

(22) Novoselov, K. S.; Geim, A. K.; Morozov, S. V.; Jiang, D.; Zhang, Y.; Dubonos, S. V.; Grigorieva, I. V.; Firsov, A. A. *Science* **2004**, *306*, 666−669.

(23) Brownson, D. A. C.; Kampouris, D. K.; Banks, C. E. *Chem. Soc. Rev.* **2012**, *41*, 6944−6976.

(24) Kim, K. S.; Zhao, Y.; Jang, H.; Lee, S. Y.; Kim, J. M.; Kim, K. S.; Ahn, J. H.; Kim, P.; Choi, J. Y.; Hong, B. H. *Nature* **2009**, *457*, 706−710.

(25) Xiang, Q. J.; Yu, J. G.; Jaroniec, M. *Chem. Soc. Rev.* **2012**, *41*, 782−796.

(26) Tu, W. G.; Zhou, Y.; Zou, Z. G. *Adv. Funct. Mater.* **2013**, *23*, 4996−5008.

(27) He, L. M.; Jing, L. Q.; Li, Z. J.; Sun, W. T.; Liu, C. *RSC Adv.* **2013**, *3*, 7438−7444.

(28) Gong, K. P.; Du, F.; Xia, Z. H.; Durstock, M. L.; Dai, M. *Science* **2009**, *323*, 760−763.

(29) Wang, Y.; Shao, Y. Y.; Matson, D. W.; Li, J. H.; Lin, Y. H. *ACS Nano* **2010**, *4*, 1790−1798.

(30) Jung, N.; Kim, N.; Jockusch, S.; Turro, N. J.; Kim, P.; Brus, L. *Nano Lett.* **2009**, *9*, 4133−4137.

(31) Geng, D. S.; Chen, Y.; Chen, Y. G.; Li, Y. L.; Li, R. Y.; Sun, X. L.; Ye, S. Y.; Knights, S. *Energy Environ. Sci.* **2011**, *4*, 760−764.

(32) Sun, Y. Q.; Li, C.; Shi, G. Q. *J. Mater. Chem.* **2012**, *22*, 12810−12816.

(33) Qu, L. T.; Liu, Y.; Baek, J. B.; Dai, L. M. *ACS Nano* **2010**, *4*, 1321−1326.

(34) Subramanian, N. P.; Li, X. G.; Nallathambi, V.; Kumaraguru, S. P.; Colon-Mercado, H.; Wu, G.; Lee, J. W.; Popov, B. N. *J. Power Sources* **2009**, *188*, 38−44.

(35) Pels, J. P.; Kapteijn, F.; Moulijn, J. A.; Zhu, Q.; Thomas, K. M. *Carbon* **1995**, *33*, 1641.

(36) Lai, L. F.; Potts, J. R.; Zhan, D.; Wang, L.; Poh, C. K.; Tang, C. H.; Gong, H.; Shen, Z. X.; Lin, J. Y.; Ruoff, R. S. *Energy Environ. Sci.* **2012**, *5*, 7936−7942.

(37) Zhang, P.; Lian, J. S.; Jiang, Q. *Phys. Chem. Chem. Phys.* **2012**, *14*, 11715−11723.

(38) Chen, P.; Xiao, T. Y.; Li, H. H.; Yang, J. J.; Wang, Z.; Yao, H. B.; Yu, S. H. *ACS Nano* **2012**, *6*, 712−719.

(39) Jia, L.; Wang, D. H.; Huang, Y. X.; Xu, A. W.; Yu, H. Q. *J. Phys. Chem. C* **2011**, *115*, 11466−11437.

(40) Wang, L.; Tian, C. G.; Wang, H.; Ma, Y. G.; Wang, B. L.; Fu, H. G. *J. Phys. Chem. C* **2010**, *114*, 8727−8733.

(41) Sun, L.; Wang, L.; Tian, C. G.; Tan, T. X.; Xie, Y.; Shi, K. Y.; Li, M. T.; Fu, H. G. *RSC Adv.* **2012**, *2*, 4498−4506.

(42) Sun, W. T.; Meng, Q. Q.; Jing, L. Q.; Liu, D. N.; Cao, Y. *J. Phys. Chem. C* **2013**, *117*, 1358−1365.

(43) Luan, Y. B.; Jing, L. Q.; Wu, J.; Xie, M. Z.; Feng, Y. J. *Appl. Catal., B* **2014**, *147*, 29−34.

(44) Ferrari, A. C.; Meyer, J. C.; Scardaci, V.; Casiraghi, C.; Lazzeri, M.; Mauri, F.; Piscanec, S.; Jiang, D.; Novoselov, K. S.; Roth, S.; Geim, A. K. *Phys. Rev. Lett.* **2006**, *97*, 187401.

(45) Pimenta, M. A.; Dresselhaus, G.; Dresselhaus, M. S.; Cancado, L. G.; Jorio, A.; Saito, R. *Phys. Chem. Chem. Phys.* **2007**, *9*, 1276−1291.

(46) Liao, L.; Zheng, Z.; Yan, B.; Zhang, J. X.; Gong, H.; Li, J. C.; Liu, C.; Shen, Z. X.; Yu, T. *J. Phys. Chem. C* **2008**, *112*, 10784−10788.

(47) Cao, Y.; Jing, L. Q.; Shi, X.; Luan, Y. B.; Durrant, J. R.; Tang, J. W.; Fu, H. G. *Phys. Chem. Chem. Phys.* **2012**, *14*, 8530−8536.

(48) Zhang, M.; Gao, G.; Zhao, D. C.; Li, Z.; Liu, F. Q. *J. Phys. Chem. B* **2005**, *109*, 9411−9415.

(49) Jing, L. Q.; Cao, Y.; Cui, H. Q.; Durrant, J. R.; Tang, J. W.; Liu, D. N.; Fu, H. G. *Chem.Commun.* **2012**, *48*, 10775−10777.

(50) Wei, X.; Xie, T. F.; Peng, L. L.; Fu, W.; Chen, J. S.; Gao, Q.; Hong, G. Y.; Wang, D. J. *J. Phys. Chem. C* **2011**, *115*, 8637−8642.

(51) Kikuchi, Y.; Sunada, K.; Iyoda, T.; Hashimoto, K.; Fujishima, A. *J. Photochem. Photobiol. A* **1997**, *106*, 51−56.

(52) Miao, X. H.; Pan, K.; Liao, Y. P.; Zhou, W.; Pan, Q. J.; Tian, G. H.; Wang, G. F. *J. Mater. Chem. A* **2013**, *1*, 9853−9861.

(53) Wang, Y. J.; Shi, R.; Lin, J.; Zhu, Y. F. *Appl. Catal., B* **2010**, *100*, 179−183.

(54) Busser, G. W.; Hinrichsen, O.; Muhler, M. *Catal. Lett.* **2002**, *79*, 49−54.

(55) Cui, H. Q.; Cao, Y.; Jing, L. Q.; Luan, Y. B.; Li, N. *ChemPlusChem* **2014**, *79*, 318−324.

(56) Wang, X. C.; Yu, J. C.; Liu, P.; Wang, X. X.; Su, W. Y.; Fu, X. Z. *J. Photochem. Photobiol. A* **2006**, *179*, 339−347.

(57) Ao, Z. M.; Li, S. *Graphene Simulation*; Intech: Rijeka, 2011.